Assessment of Metal Impurity Partitioning and Speciation in Mineral Carbonation Processes Using FGD-Gypsum from Coal-Fired Power Plants under Distinct Operating Conditions

Patricia Córdoba*

Read Online

ACCESS | 📊 Metrics & More | 📧 Article Recommendations | 🅢🅘 Supporting Information

ABSTRACT: The sequestration of carbon dioxide (CO_2) stands as a profoundly pivotal environmental challenge, given its potential to directly contribute to the advancement of environmental, societal, and economic objectives across a multitude of nations. In the present study, we have conducted an evaluation of the metal impurity partitioning and speciation in mineral carbonation processes conducted in laboratory using flue gas desulfurization (FGD) gypsums originating from both Spanish and two Chinese coal-fired power plants, each subject to distinct fuel sources and FGD operational conditions. Of the three resultant carbonation products, two exhibited $CaCO_3$ content in the range of 81−83%, while the third registered 76.9% $CaCO_3$ content—a variance

attributed to the occurrence of metallic impurities within the initial FGD-gypsum. The partitioning and speciation of metal impurities at all stages of CO_2 conversion have enabled us to proffer four potential reaction mechanisms governing carbonation efficiency: (i) conversion of metal sulfates to metal carbonate complexes, (ii) transformation of transferable elements into metal oxides and oxyhydroxide complexes, (iii) transformation of metal sulfates into diverse metal complexes, and (iv) diverse pathways of elemental transformation. Metal impurities present in FGD-gypsum lead to the formation of complexes between As and metals, thereby affecting their activity. Higher Ca/Mn, Ca/Fe, and Ca/Al ratios in one FGD-gypsum slurry enhance $Ca_3(AsO_4)_2 \cdot 8H_2O$ activity, while in another, excess Ca facilitates $Mn_3(AsO_4)_2 \cdot 8H_2O$ formation during carbonation, with coprecipitation retaining As in carbonation products. The occurrence of metallic contaminants in FGD-gypsums may exert a substantial influence on the effectiveness of CO_2 conversion, thereby impacting the feasibility of using resultant carbonation products, with potential implications for environmental leaching and diminished reusability prospects.
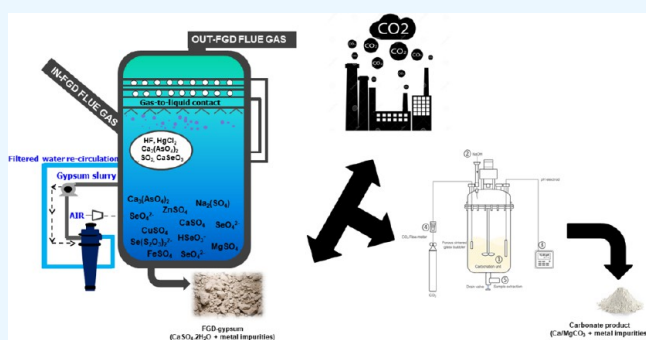
1. INTRODUCTION

In defiance of global financial incentives to transition toward renewable energies, China initiated the construction of coal power capacity amounting to 50 gigawatts (GW) in 2022.[1] Many of these projects were newly permitted and expedited for construction, marking a return to pre-COVID-pandemic levels and equating to nearly one new coal-fired power plant per week.[1] In Europe, where coal mining activities had been gradually reduced due to the European Union's (EU) policy to shift toward a lower carbon economy, the energy crisis stemming from the Russo-Ukrainian war led to a partial resurgence in coal-fired power plant usage.[2] This was due to natural gas restrictions and disruptions in supply from Russia to Western countries. Consequently, the world is currently grappling with two distinct scenarios. On a global scale, coal power generation continues to contribute significantly to atmospheric pollution, particularly carbon dioxide (CO_2), the major greenhouse gas (GHG) accountable for driving global warming, as well as poor air quality.[3] Additionally, coal combustion results in the generation of large volumes of residues, known as coal combustion products

(CCPs), which further exacerbate climate change and local environmental issues. At the local level, coal power generation has been associated with land degradation and contamination. In this context, should China persist in its reliance on coal-based power generation and the energy crisis in Europe endure, atmospheric pollution and land degradation will remain significant environmental challenges in developing countries.

In efforts to mitigate CO_2 emissions, various carbon capture and storage (CCS) technologies have been developed.[4] Among these, mineral carbonation has emerged as a highly promising option. This technology enables the capture of CO_2 by transforming it into stable and environmentally benign

carbonates through direct reaction with calcium (Ca)- and/or magnesium (Mg)-bearing minerals.[4−6]

Waste gypsum, composed mainly of $CaSO_4 \cdot 2H_2O$,[7] originates from various industrial processes including phosphogypsum (PG), red gypsum (RG), and flue gas desulfurization gypsum (FGD).

Phosphogypsum (PG) is produced as a byproduct during the manufacture of phosphoric acid (H_3PO_4) from phosphate rock containing apatite [$Ca_5(PO_4)_3OH$], reacted with sulfuric acid (H_2SO_4). Although a small amount is used in construction or agriculture, most is stockpiled, posing environmental challenges in preventing water contamination. Gypsum waste shows potential for CO_2 capture, with estimates suggesting that it could sequester several hundred megatonnes. Research by Mattila and Zevehoven[8] found that mineral carbonation of PG achieved over 95% conversion of Ca to $CaCO_3$, though the resultant precipitates contained contaminants such as rare earth metals and sulfur (S). Red gypsum is a waste product from the titanium dioxide (TiO_2) manufacturing process using ilmenite as a raw material. Titanium dioxide pigment is produced via sulfate or chloride-ilmenite processes.[9] Typically, red gypsum is mixed with water into a slurry and disposed of in nearby landfills. It consists mainly of hydrated $CaSO_4$ (70 wt %), Fe_2O_3 (30 wt %), and minor Al_2O_3.[10] Azdarpour et al.[11] studied its properties and direct aqueous mineral carbonation, showing that resulting carbonates were primarily CaO, Fe_2O_3, and SO_3, with some impurities. However, the study highlighted challenges in achieving high purity and efficiency in carbonate formation through direct aqueous processes.

Wet FGD byproducts result from complex acid-based reactions to capture sulfur dioxide (SO_2), occurring via forced or natural oxidation.[12] Naturally oxidized byproducts consist mainly of a sludge mixture containing about 50−60% calcium sulfite hydrate ($CaSO_3 \cdot 1/2H_2O$) and calcium sulfate dihydrate ($CaSO_4 \cdot 2H_2O$), posing dewatering challenges due to its consistency. In contrast, under forced oxidation, the final product is about 90% $CaSO_4 \cdot 2H_2O$,[12] known as FGD-gypsum. In 2019, coal-fired power plants globally produced an estimated 176 million tons per annum (Mt/a) of FGD-gypsum. Approximately 128.1 Mt/a was used, while the surplus was either directed to reclamation sites, stored for future use, or disposed of alongside other CCPs.[13]

FGD-gypsum, comprising finely grained Ca-bearing minerals, is a promising alternative to other Ca-rich substances in carbonation processes conducted in laboratory settings. In these processes, CO_2 interacts with either natural minerals or industrial waste materials containing Ca, forming stable carbonates—a method termed ex situ carbonation, extensively studied in the mineral technology literature.[14−23] Reviews have covered the historical and current status of both in situ and ex situ mineral carbonation for CO_2 storage.[21−23] Although direct FGD-carbonation processes yield high $CaCO_3$, the free $CaCO_3$ presence is limited due to crucial carbonation parameters such as temperature, solid-to-liquid ratio, and pressure conditions,[22−26] often neglecting metal impurity distribution (e.g., Al, Fe, Si, Sr, Y, Ni, Mn, Cl, Pb, and U) in parent FGD-gypsums and their potential impact on CO_2 capture into stable, environmentally benign carbonates. The presence of metal impurities in FGD-gypsums is influenced by various factors, including the composition of the feed fuel or fuel blend (e.g., petroleum coke serving as a source of HCl and Ni), the effectiveness of particulate control measures (e.g., a small fraction of fly ash may bypass controls and reach the FGD system), and the operational conditions of the FGD system (e.g., the preference for water recirculation to the scrubber from gypsum slurry filtration in some power plants, which can result in the retention of metal impurities in FGD-gypsums).[22] In my recent study,[27] we examined the utilization of commercially sourced FGD-gypsum obtained from a copper smelting operation in CO_2 mineral carbonation. This differs from FGD-gypsum produced as a byproduct of coal-fired power generation. Our findings highlighted the significant impact of metallic contaminants on CO_2 conversion efficiency, affecting the feasibility and environmental implications of resulting carbonate products. The leaching of As exceeded safe levels in the carbonate end-products, emphasizing the need to address metal impurities in FGD-gypsum before its use as a calcium source for CO_2 conversion. This underscores the importance of studying metal impurity effects on mineral carbonation, including their distribution and forms, to evaluate CO_2 capture feasibility and potential reuse of carbonates. Such research is crucial for identifying environmental concerns and guiding decisions on CO_2 capture and utilization strategies.

This paper introduces an investigation focusing on three pivotal aspects. First, it delves into scrutinizing the feasibility of CO_2 mineralization via carbonation processes conducted in laboratory leveraging FGD-gypsums from a Spanish plant and two Chinese coal-fired power plants, each operating under distinct fuel compositions and FGD conditions. This analysis provides unprecedented insights into the intricate interplay of variables shaping metal impurity dynamics. Second, the study probes into the partitioning, speciation, and fate of these metal impurities, highlighting their potential retention in the carbonation products or their dissolution into carbonation aqueous phases. Third, a particular examination of As speciation is performed throughout each carbonation process to delineate its dynamics. By shedding light on these fundamental processes, this research not only advances our understanding of CO_2 conversion mechanisms but also offers valuable guidance for optimizing carbon capture strategies and mitigating environmental risks associated with metal impurities.

2. MATERIALS AND METHODS

2.1. FGD-Gypsum Sample Collection and Analysis. For the investigation in this study, FGD-gypsum samples come from three coal-fired power plants, comprising one located in Spain[28] and two in China,[29] all of which were equipped with a wet FGD system employing forced oxidation. Within the study, the Spanish facility is identified as PP1, while the two Chinese plants are designated as PP2 and PP3, respectively.

Sampling at PP1 (1200 MW) was conducted while the plant was supplied with a coal/petroleum coke blend at a ratio of 56:44 (%w/w).[28] At PP2 (1000 MW), sampling took place while utilizing a blend of lignite coal and petroleum coke at a ratio of 60:40 (%w/w).[29] PP2 is equipped with bag filters (BF) and a wet limestone-based FGD system, where limestone serves dual purposes: creating the fluidized bed in the combustion unit and acting as a neutralizer material for desulfurization. Last, sampling at PP3 (670 MW)[29] was carried out with the power plant exclusively fed with local anthracite coal. At PP1, four sample sets of FGD-gypsum were obtained through two samplings per day over two consecutive days in 2018. Conversely, at PP2 and PP3, two sample sets were collected each, with one sampling per day over a 2-day period for FGD-gypsum in 2019. The gathered samples were stored in PVC bottles for subsequent analysis at IDÆA-CSIC.

Upon receipt, FGD-gypsum samples (10 kg) underwent homogenization, followed by drying at 60 °C and subsequent division for further examination. A fraction of each homogenized sample underwent air-drying at laboratory temperature for mercury (Hg) analysis, while another fraction was subjected to duplicate acid digestion using a specialized two-step method.[30] The concentrations of major elements in the acid digests were determined using Inductively Coupled Plasma Atomic-Emission Spectrometry (ICP-AES), employing the Iris Advantage Radial ER/S device from Thermo Jarrell-Ash. For the analysis of trace elements, Inductively Coupled Plasma Mass Spectrometry (ICP-MS) was employed, utilizing the X-SERIES II instrument from Thermo Fisher Scientific in Bremen, Germany. This ICP-MS system featured a collision cell to eliminate spectral interferences and used 10 μg/L In as the internal standard. Reagent blanks and standard reference materials (NIST SRM 1633b) were processed alongside the samples to ensure analytical accuracy.

X-ray diffraction (XRD) diffractograms were generated utilizing a Bruker D8 A25 Advance diffractometer with $\theta-\theta$ geometry, CuKα1 radiation, and a position-sensitive LynxEyeXE detector. The XRD scans were conducted with an applied voltage of 40 kV and a current of 40 mA. The scanning range spanned from 4 to 60° of 2θ, with a step size of 0.019°, and each step was counted for 0.1 s to maintain the sample in continuous rotation at a rate of 15 rotations per minute. The identification of crystalline phases was performed using EVA software.

The particle resolved composition and morphology of FGD-gypsum and carbonation products were investigated using a Field Emission Scanning Electron Microscope (FE-SEM) JEOL JSM-7001F with secondary and retro-dispersed electron detectors and polaron critical point dryer, equipped with X-ray energy dispersive spectroscopy (EDX). FE-SEM analysis results can assist in gaining a clearer understanding of the distribution of metal impurities by providing high-resolution images that reveal the spatial arrangement and concentration of these impurities within a sample, allowing to visualize the surface morphology and elemental composition of materials at a microscale, thereby helping to identify where and how metal impurities are distributed across a sample.

2.2. Carbonation Process. The carbonation batch experiments and methodology outlined herein have undergone laboratory-scale validation, confirming their reliability.[27] The experimental procedure involves the introduction of CO_2 into slurries laden with FGD-gypsum using 100% CO_2 gas regulated by a calibrated flowmeter. In the reactor, an impeller stirred the FGD-gypsum slurries, which were prepared using Milli-Q water. The temperature was upheld under ambient laboratory conditions, and experiments were carried out under atmospheric pressure. The study aimed to create alkaline conditions (pH ≈ 12.0) to reduce metal leaching from FGD-gypsum and promote $Ca(OH)_2$ formation. At the onset of each carbonation procedure, 125 mL of 4 M NaOH was added to the vessel. After a 20 min wait, CO_2 was introduced at 5 min intervals over 5 min, maintaining 0.5 g/L CO_2 flow rate. The pH was continuously monitored using a Thermo Scientific Orion 410A pH meter, and NaOH additions were made at intervals of pH stability over the next 20 min. Experiments ended after 70 min. Nine trials (3 per FGD-gypsum sample) evaluated CO_2 conversion. Slurry samples (10 mL) were taken every 5 min. Additional details of the experimental conditions are detailed in Table S1, Supporting Information.

The resultant carbonation products underwent analysis through XRD and acid digestion employing the previously mentioned specialized two-step digestion technique[23] for subsequent ICP analyses. The carbonation conversion efficiency was assessed via thermogravimetric analysis (TGA-SDTA 851e, Mettler Toledo) under a nitrogen atmosphere, with a heating rate of 10 °C/min up to 900 °C, utilizing an aluminum crucible.

In this investigation, the purity of the carbonation products was assessed through the determination of weight loss (ΔW, %) via thermogravimetric analysis (TGA). The calculation involves considerations of the molecular weights of CO_2 ($MwCO_2$) and $CaCO_3$ ($MwCaCO_3$). The purity of $CaCO_3$ within the carbonation end-products was ascertained using the computational methodology outlined by Lee et al.:[31]

$$P_{CaCO_3}(\%) = \frac{\Delta W(\%) x Mw_{CaCO_3}}{Mw_{CO_2}}$$

2.3. Partitioning. When evaluating the distribution and fate of trace elements within laboratory-based carbonation processes, it is beneficial to estimate overall partitioning across the various streams. To calculate trace element partitioning accurately, it is imperative to consider all pertinent streams within the carbonation unit, including inputs such as the FGD-gypsum slurry and CO_2 gas flow and outputs such as the carbonation products and the aqueous phase of the carbonation products. Preferably, partitioning is determined by measuring flow rates and trace element concentrations in all streams and establishing the ratio of total outgoing to incoming flows. This approach fulfills three main objectives within this investigation: first, assessing process feasibility by scrutinizing the precision of each carbonation process conducted in the laboratory, thereby validating their efficiency; second, conducting a feasibility appraisal to ascertain the potential utilization of FGD-gypsum for CO_2 capture; and third, the assessment of metallic impurity distribution inherent in FGD-gypsum. This partitioning methodology has been corroborated in both industrial[32−34] and laboratory-scale settings.[27] Flow rates of input and output streams involved in the CO_2 conversions are provided in Table S2 (Supporting Information).

2.4. Geochemical Modeling. Simulation methodologies are extensively used across an array of academic domains, encompassing different fields of application. These tools play a pivotal role in streamlining the modeling, integration, and optimization of processes.[35]

The complete carbonation experiments conducted at the laboratory scale were subjected to a three-stage modeling process using the PHREEQC code coupled with the LLNL thermodynamic database.[36] Initially, the distribution of aqueous species within the gypsum slurries and their saturation state relative to a predefined set of minerals were examined. This involved using input data such as the chemical composition as well as the temperature (50−60 °C) and pH of the aqueous $CaSO_4 \cdot 2H_2O$ slurries. Second, based on the results of the first simulation, we modeled the incremental addition of NaOH to the gypsum slurries. The intervals for NaOH addition were calculated based on the total moles of NaOH added. The third simulation entailed the injection of CO_2 gas phase, characterized by experimental pressure, volume, and temperature data. This simulation used the outcomes from the first two simulations. The culmination of these simulations resulted in the conversion of speciation and distribution of aqueous species from the gypsum slurries to carbonation slurries and products.
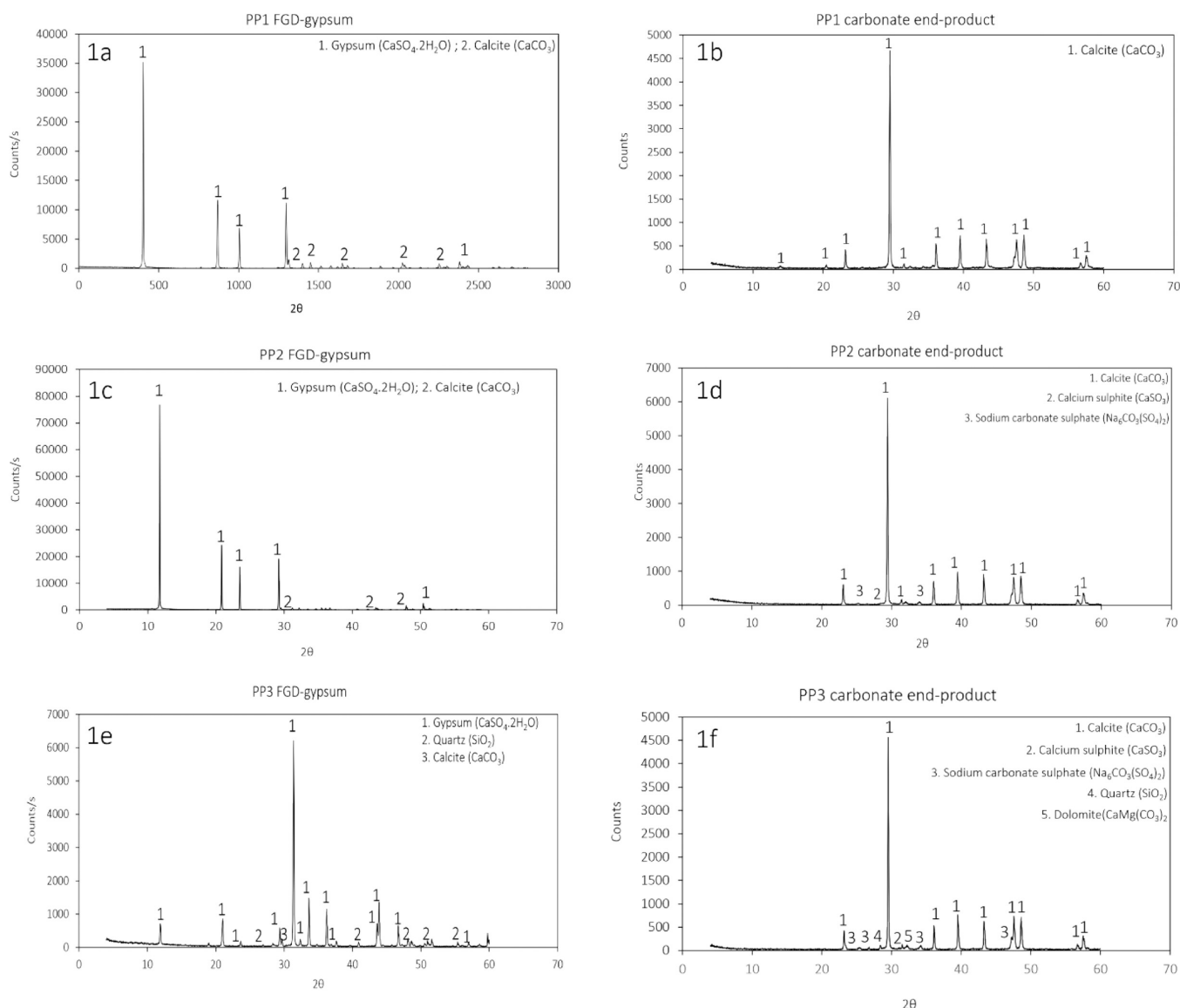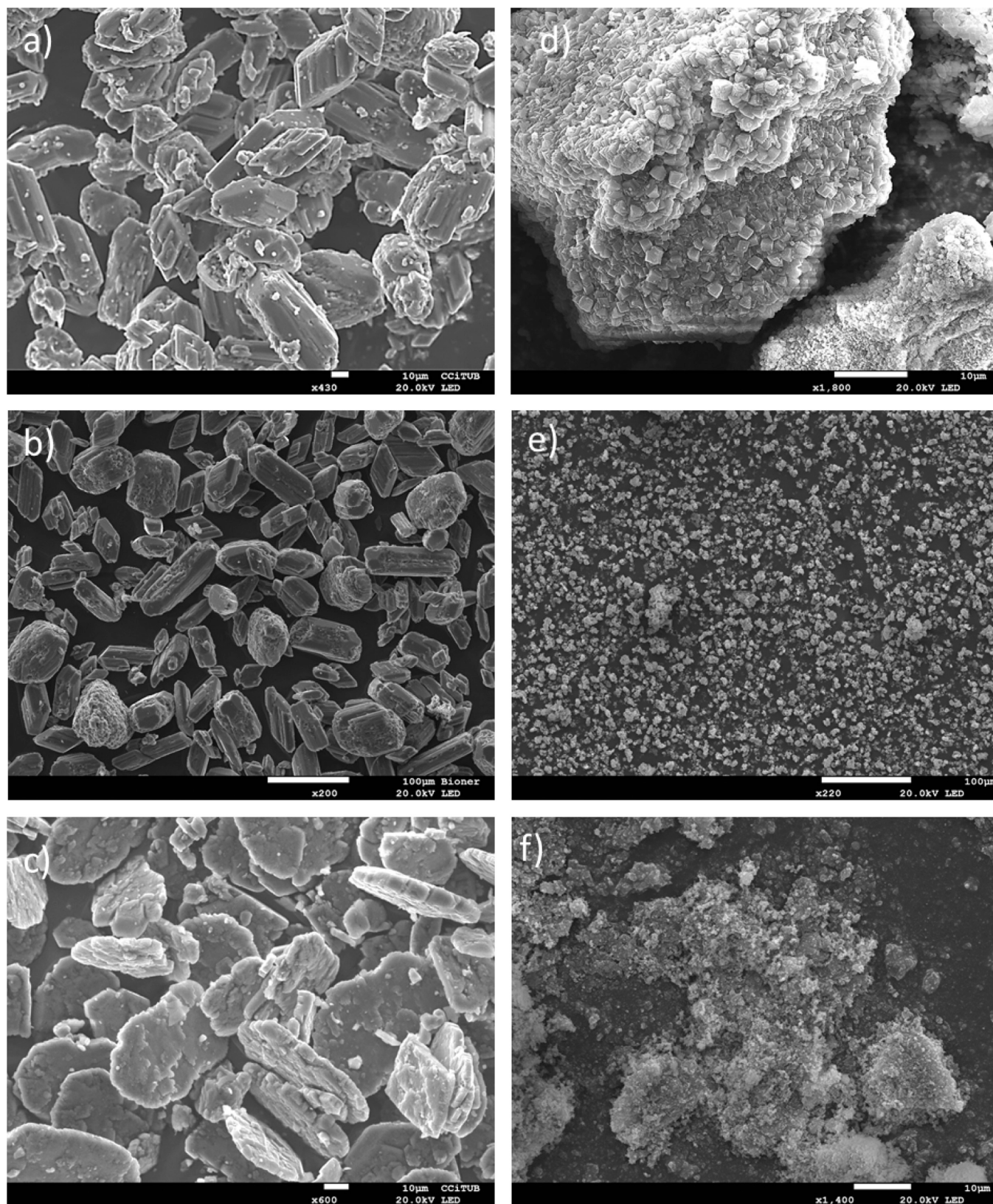
Figure 1. Diffractogram of PP1 FGD-gypsum (a), PP1 carbonation product (b), PP2 FGD-gypsum (c), PP2 carbonation product (d), PP3 FGD-gypsum (e), and PP3 carbonation product (f).

3. RESULTS AND DISCUSSION

3.1. Characterization of FGD-Gypsums. Gypsum $(CaSO_4 \cdot 2H_2O)$ with minor levels of calcite $(CaCO_3)$ was identified as the primary crystalline phase in the FGD-gypsum samples from PP1 and PP2 (Figure 1a,c). SEM-EDX analyses (Figure 2a,c) revealed the distinctive prismatic tubular shape of both FGD-gypsum samples, with a notable presence of FA spheres and associated Al–Si matrix particles observed on the surface of the PP1 FGD-gypsum. In contrast, the FGD-gypsum from PP3 exhibited gypsum $(CaSO_4 \cdot 2H_2O)$ as the predominant crystalline phase, alongside minor concentrations of calcite $(CaCO_3)$ and quartz (SiO_2) (Figure 1e).

PP1 FGD-gypsum exhibited notable concentrations of Mn and Sr within the range of 201−627 mg/kg, along with trace levels of Ti, V, Ni, and Cu (Table 1). While electrostatic precipitators (ESPs) generally attain retention efficiencies exceeding 99%, the actual collection efficiency fluctuates due to factors such as particle size, ash resistivity, flue gas temperature, and moisture content.[37] Efficiency is notably lower within the particle size range of 0.1−1.5 μm, with some FA

potentially evading controls and entering the FGD system.[38] PP1 operates with both an ESP and recirculation of FGD waters to the scrubber, which is identified as the primary factor contributing to the accumulation of inorganic trace pollutants in these waters.[39] The elevated pH of both limestone slurry and FA in the FGD facilities the dissolution of these elements, along with others such as Se, As, Sb, and V, when flue gas passed through the sprayers.[39] Once saturation is attained in the aqueous phase of the gypsum slurry, these elements have a propensity to precipitate or coprecipitate within the FGD-gypsum. Comparatively, trace elements were present in lower quantities in the FGD-gypsums from PP2 and PP3, except for Sr (738 mg/kg), which also exhibited a significant concentration in the PP3 FGD-gypsum. The elevated concentration of Sr in the PP3 FGD-gypsum may be attributed to the limestone used in the desulfurization process, which could potentially contain impurities of strontianite $(SrCO_3)$. The presence of these impurities in the FGD-gypsums could potentially transfer to the carbonation end-products. Hence, this study evaluates the partitioning of trace elements during CO_2 conversion.

Figure 2. Scanning electron microscope (SEM) photomicrographs of PP1 FGD-gypsum (a), PP1 carbonation product (b), PP2 FGD-gypsum (c), PP2 carbonation product (d), PP3 FGD-gypsum (e), and PP3 carbonation product (f).

3.2. Process of CO₂ Mineral Carbonation. *3.2.1. Carbonation Products.* The carbonation products from the conversion of PP1 FGD-gypsum manifest as a single-phase calcite, as evidenced by XRD findings (Figure 1b). PP1 FGD-

gypsum, which was prismatic tubular configured with a substantial quantity of FA particles, was transformed into calcite with a well-defined rhombohedral shape as shown by the SEM-EDX photomicrographs (Figure 2d). Consequently, an

Table 1. Chemical Composition of PP1, PP2, and PP3 FGD-Gypsums and PP1, PP2, and PP3 Carbonation End-Products[a]

		PP1		PP2		PP3	
		FGD-gypsum	CP	FGD-gypsum	CP	FGD-gypsum	CP
%							
	Al_2O_3	0.150	0.143	0.104	0.129	0.229	0.252
	CaO	31.1	45.8	31.4	47.1	40.6	45.0
	Fe_2O_3	0.108	0.069	0.042	0.070	0.133	0.152
	K_2O	<dl	<dl	0.029	<dl	0.084	<dl
	MgO	0.885	0.642	0.040	0.329	0.234	0.277
	Na_2O	0.027	6.60	0.017	5.43	0.013	6.98
	SO_3	42.0	3.06	46.5	5.11	57.8	6.42
mg/kg							
	Li	2.17	1.75	<dl	<dl	0.835	<dl
	Be	<dl	<dl	<dl	<dl	<0.01	<dl
	B	155	<dl	13.4	<dl	18.7	<dl
	Sc	<dl	<dl	<dl	<dl	<dl	<dl
	Ti	41.9	34.2	39.5	63.2	59.5	63.4
	V	25.0	17.6	2.17	2.95	2.57	2.65
	Cr	1.61	2.23	8.84	14.0	17.2	20.3
	Mn	201	305	12.7	18.3	10.1	10.9
	Co	0.394	<dl	<dl	<dl	<dl	<dl
	Ni	9.13	<dl	0.651	<dl	0.764	<dl
	Cu	2.24	<dl	<dl	<dl	0.788	<dl
	Ga	<dl	<dl	<dl	<dl	<dl	<dl
	Ge	<dl	<dl	<dl	<dl	<dl	<dl
	As	1.55	15.9	1.13	<dl	1.26	<dl
	Se	1.13	<dl	<dl	<dl	2.59	1.48
	Rb	1.33	1.13	<dl	<dl	2.06	2.16
	Sr	627	963	105	153	738	855
	Y	2.06	2.75	2.35	3.79	1.41	1.68
	Zr	0.203	<dl	1.67	<dl	3.51	<dl
	Nb	<dl	<dl	<dl	<dl	<dl	<dl
	Mo	0.862	<dl	<dl	<dl	<dl	<dl

		PP1		PP2		PP3	
		FGD-gypsum	CP	FGD-gypsum	CP	FGD-gypsum	CP
	Cd	<dl	<dl	<dl	<dl	<dl	<dl
	Sn	1.96	3.43	<dl	<dl	<dl	<dl
	Sb	<dl	<dl	<dl	<dl	<dl	<dl
	Cs	<dl	<dl	<dl	<dl	<dl	<dl
	Ba	10.7	12.5	28.3	41.1	7.53	7.83
	La	0.891	1.10	1.14	1.47	1.23	1.22
	Ce	1.21	1.49	0.878	1.40	1.92	2.34
	Pr	<dl	<dl	<dl	<dl	<dl	<dl
	Nd	<dl	<dl	0.733	1.07	1.15	1.15
	Sm	<dl	<dl	<dl	<dl	<dl	<dl
	Eu	<dl	<dl	<dl	<dl	<dl	<dl
	Gd	<dl	<dl	<dl	<dl	<dl	<dl
	Tb	<dl	<dl	<dl	<dl	<dl	<dl
	Dy	<dl	<dl	<dl	<dl	<dl	<dl
	Ho	<dl	<dl	<dl	<dl	<dl	<dl
	Er	<dl	<dl	<dl	<dl	<dl	<dl
	Tm	<dl	<dl	<dl	<dl	<dl	<dl
	Yb	<dl	<dl	<dl	<dl	<dl	<dl
	Lu	<dl	<dl	<dl	<dl	<dl	<dl
	Hf	<dl	<dl	<dl	<dl	<dl	<dl
	Ta	<dl	<dl	<dl	<dl	<dl	<dl
	W	<dl	<dl	<dl	<dl	<dl	<dl
	Tl	<dl	<dl	<dl	<dl	<dl	<dl
	Pb	1.39	1.57	<dl	<dl	1.35	0.485
	Bi	<dl	<dl	<dl	<dl	<dl	<dl
	Th	<dl	<dl	<dl	<dl	<dl	<dl
	U	1.38	1.27	<dl	<dl	1.18	<dl

[a]CP: carbonate product.

anticipated weight loss due to the release of a CO_2 molecule should occur within the temperature interval of 600−800 °C.[40] In Figure 3a, the thermogram of the carbonation product from PP1 FGD-gypsum exhibits a distinctive thermal event spanning from 607.5 to 760 °C, with the highest peak observed at 714.57 °C, corresponding to the decomposition of $CaCO_3$ and emission of CO_2, resulting in a weight loss of 36.6%. The carbonation product from PP1 FGD-gypsum comprises 83.2% $CaCO_3$ (Table 2).

XRD analysis revealed traces of calcium sulfite ($CaSO_3$) and sodium carbonate sulfate ($Na_6CO_3(SO_4)_2$) in addition to $CaCO_3$ in the carbonation product from PP2 FGD-gypsum (Figure 1d). Calcite was the primary crystalline phase in the carbonation product from PP3 FGD-gypsum (Figure 1e), along with traces of calcium sulfite ($CaSO_3$), sodium carbonate sulfate ($Na_6CO_3(SO_4)_2$), dolomite ($CaMg(CO_3)$), and quartz (SiO_2). PP2 FGD-gypsum transformed into calcite, exhibiting irregular grains and undefined shapes (Figure 2e), while PP3 FGD-gypsum was only partially transformed into calcite, displaying grain agglomerations. This large amount of agglomeration, as shown in Figure 2f photomicrographs, suggests that it is probably formed via reprecipitation of dissolved matter at particle contact points by forming interparticle necks.[41] This event may have occurred during the filtration and further drying of the carbonation slurry (carbonate end-product), as dissolved aqueous complexes (e.g., Na_2SO_4 and $NaCO_3^-$) become

gradually more concentrated and eventually exceed their solubility limit.

The carbonation products from PP2 and PP3 FGD-gypsums demonstrate singular thermal events within the temperature interval of 600−800 °C, demonstrating thermal decomposition of $CaCO_3$ and resultant weight losses of 35.6 and 33.8%, respectively (Figure 3b,c). However, the carbonate end-products from PP2 and PP3 FGD-gypsums contain 81.0 and 76.9% $CaCO_3$, respectively, indicating a lower conversion efficiency for PP3 FGD-gypsum (Table 2).

Although the carbonation product from the PP1 FGD-gypsum contains 83.2% $CaCO_3$, a proportion relatively higher than that found in the carbonation product from the PP2 FGD-gypsum (81.0%) and significantly higher than that in the carbonation product from the PP3 FGD-gypsum (76.9%), this carbonate exhibits notable concentrations of trace elements, particularly Ti, Mn, As, Sr, Sn, and Ba (Table 1). In contrast, alongside the unreacted gypsum, the PP3 carbonation product reveals noteworthy concentrations of certain elements, including Al (0.252% as Al_2O_3), Fe (0.152% as Fe_2O_3), and Na (6.98% as Na_2O), with smaller content of Cr (20.3 mg/kg), Zn (48.7 mg/kg), Pb (31.6 mg/kg), Cu (23.6 mg/kg), Cd (14.9 mg/kg), and Sn (10.7 mg/kg). A clear visual representation of the impact of metal impurities on carbonation efficiency is provided in the charts included in the Supporting Information (Figure S1). These charts compare the content of metal impurities and $CaCO_3$ for each of the cases studied.
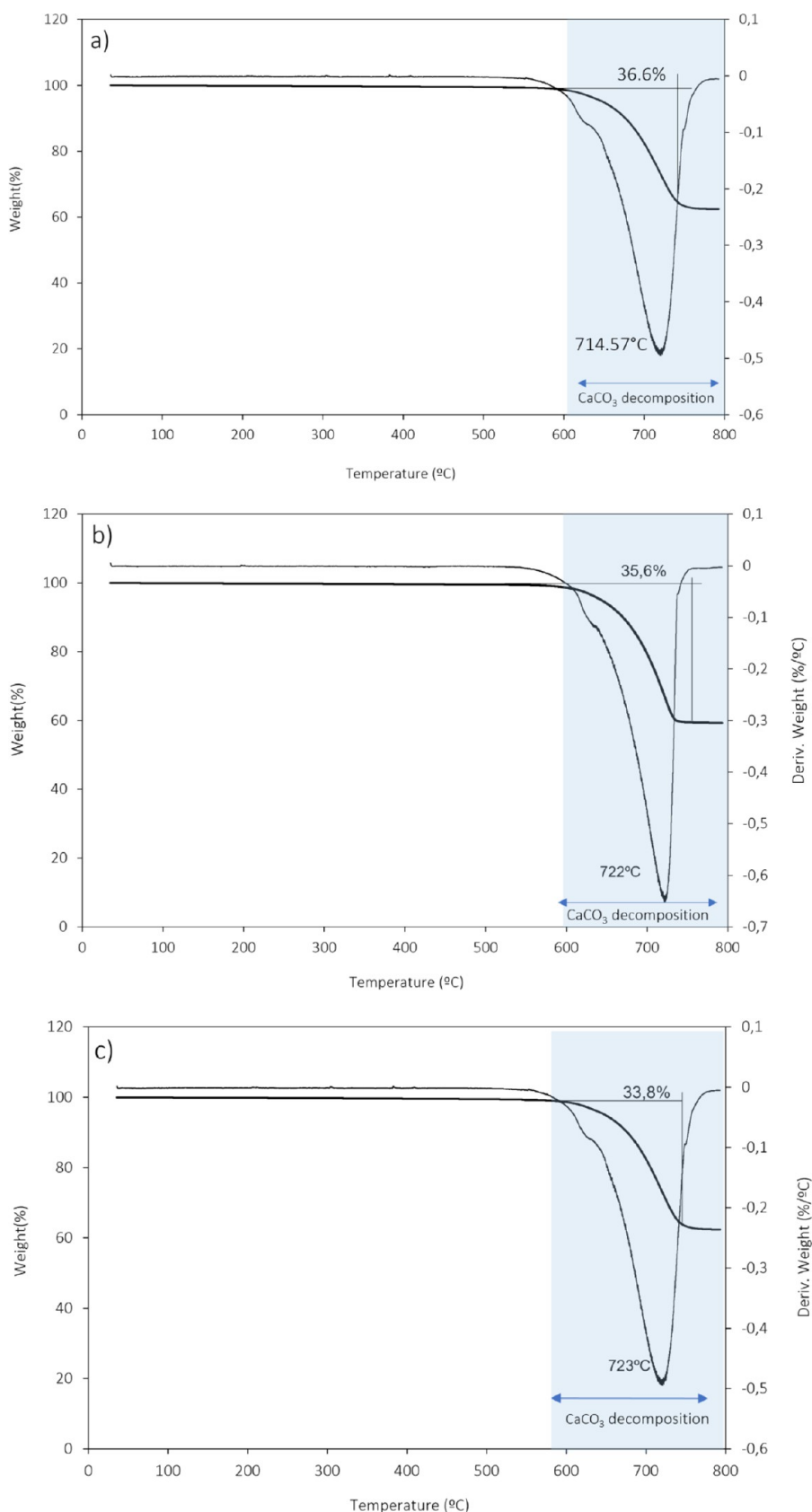
Figure 3. Thermograms of the PP1 (a), PP2 (b), and PP3 (c) carbonation products.

Three factors, to be elaborated on in the subsequent section, could account for these findings. First, impurities inherited from the parent FGD-gypsum do not dissolve during the carbonation process, further contributing to the lower $CaCO_3$ purities. Second is the ionic strength (IS) of the FGD-gypsum slurries, as most metallic impurities are introduced into the carbonation

Table 2. Carbonation Efficiencies of the PP1, PP2, and PP3 CO_2 Conversion Processes[a]

	PP1		PP2		PP3	
	FGD-gypsum	CP	FGD-gypsum	CP	FGD-gypsum	CP
%CaO	31.1		31.4		40.6	
%CO_2 release		36.6		35.6		33.8
%$CaCO_3$	55.5	56.0	72.5	83.2	81.0	76.9
Exp. Mass (g)	16.0	16.0	16.0	10.3	10.6	10.0
Ce (%)		96.3		95.9		66.5

[a]CP: carbonation product. %CaO in FGD-gypsums is obtained from ICP-AES. CO_2% in the carbonate end-products is obtained from TGA results. %$CaCO_3$ calculated from %CO_2 data. Mass (g) of samples in the experiment.

process from the parent FGD-gypsum matrix. Hence, this could potentially decrease the transfer of CO_2 (g) from the gas phase to the aqueous phase. Third, the pH and speciation of trace elements during CO_2 conversion might also be influential.

3.2.2. Aqueous Phases. Initially, under nonalkaline conditions, Mg and Ca coexist in the PP1 FGD-gypsum slurry with decreasing activity order, $MgSO_4$ > Mg^{2+} > Ca^{2+} > $CaSO_4$ aqueous complexes, while in the PP2 and PP3 FGD-gypsum slurries, they exist as Ca^{2+} > Mg^{2+} > $CaSO_4$ aqueous complexes. However, the $CaNO_3^+$ complex also exhibits high activity in the PP3 FGD-gypsum slurry. Upon the addition of NaOH (aq) to the carbonation unit, alkaline conditions were introduced into the aqueous phases of the PP1 (pH 13.19), PP2 (pH 12.77), and PP3 (pH 12.77) FGD-gypsum slurries (Figure 4), leading to the formation of $CaOH^+$ and $NaSO_4^-$ aqueous complexes.

During CO_2 conversion, CO_2 (g) is injected into the carbonation unit, where it diffuses from the gas to the aqueous phase and hydrolyses to H_2CO_3 (aq), immediately dissociating into HCO_3^- (aq) and CO_3^{2-} (aq) in two successive dissociation stages. The stability region of HCO_3^- (aq) leads to the coexistence of Mg predominantly as $MgHCO_3^-$ along, in decreasing activity order, with $NaHCO_3$ > $MgCO_3$ > $MnCO_3$ >

$CaHCO_3^+$ > $MnHCO_3^+$ in the PP1 carbonate slurry. Calcium as Ca^{2+} along with $CaHCO_3^+$ > $CaSO_4$ > $CaCO_3$ predominates in the PP2 carbonate slurry and with $CaHCO_3^+$ > $CaSO_4$ > $CaNO_3^+$ in the PP3 carbonate slurry. The critical stage occurs when the $CaCO_3$ aqueous complex is established within the CO_3^{2-} stability domain. Upon reaching saturation, precipitation occurs as $CaCO_3$ (s), leading to the pH approaching a constant value (Figure 4), indicating the culmination of CO_2 conversion into $CaCO_3$.

Based on the modeling of CO_2 conversions and the examination of carbonate end-products, it can be inferred that the elevated concentration of trace elements in the PP1 carbonation product may result from extensive formation of metal-HCO_3 or metal-CO_3 solid phases, owing to the substantial presence of metal impurities in the PP1 FGD-gypsum matrix. Conversely, in the case of the PP3 CO_2 conversion, the comparatively lower content of $CaCO_3$ compared to PP1 and PP2 may be attributed to (i) the presence of impurities, such as SiO_2 inherited from the parental FGD-gypsum, which remains undissolved, and intermediate phases formed during the carbonation process, as indicated by XRD analysis, and (ii) the significant influx of NO_3^- during the CO_2 conversion process, leading to competition with SO_4^{2-}, HCO_3^-, and CO_3^{2-} for association with Ca ions, as well as an increase in IS.

The input of NO_3^- during the PP3 CO_2 conversion originates from the dissolution of NO_3 species present in the PP3 FGD-gypsum. To understand why these species are retained in the FGD-gypsum, it is necessary to revisit the desulfurization process, which yields this byproduct. The FGD system encompasses several water streams that can normally be categorized into two groups: (i) noninvolved waters in FGD and (ii) FGD water streams.[39] These wastewater streams, besides containing SO_4^{2-} and Cl^-, exhibit a significant concentration of nitrogen in several forms, with NO_3^- being the predominant component, constituting 70% of the total nitrogen content. Additionally, elevated levels of ammonium nitrogen, reaching up to 600 gN-NH_4/m³, and nitrate nitrogen up to 200 gN-NO_3/m³, have been observed.[42] Upon saturation of nitrate aqueous complexes in the aqueous phase of the
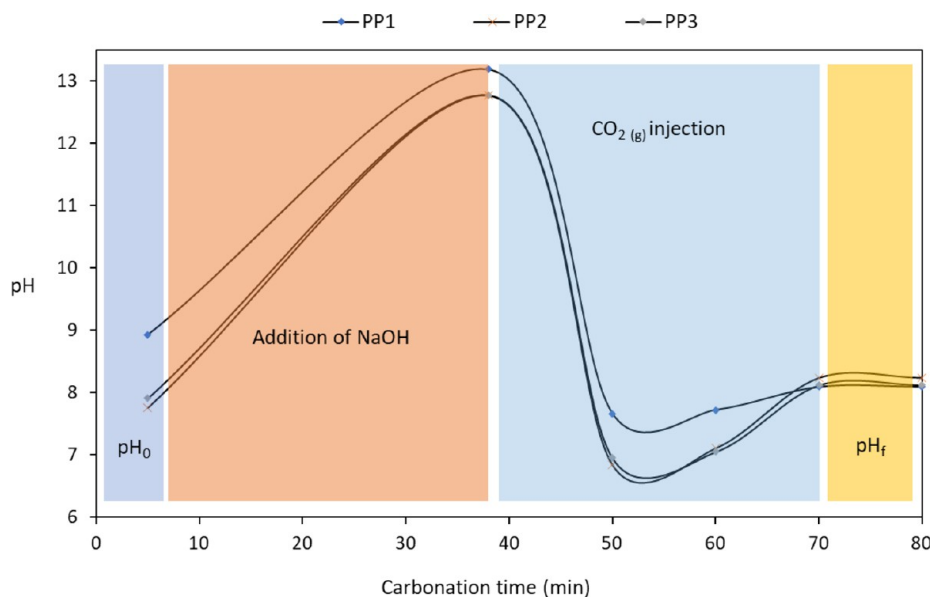
Figure 4. pH evolution during the PP1, PP2, and PP3 CO_2 conversions.

gypsum slurry, precipitation or coprecipitation within the FGD-gypsum is observed. Hence, during the prestage of CO_2 conversion when an FGD-gypsum slurry is created, solid species, including NO_3 species, dissolve in the aqueous phase of the gypsum slurry, concurrently leading to an increase in the ionic strength.

Various models have been investigated to explore the reduction in CO_2 solubility in aqueous solutions with different compositions due to changes in IS. While some focus on simple NaCl solutions, solutions from industrial activities, containing major ions (cations and ions) in solution, are more complex. Research[43] examining the influence of electrostricted water and ion hydration thermodynamics in aqueous solutions containing major ions found that CO_2 solubility declines with increasing IS. Furthermore, another study,[44] integrating six sophisticated models (289 laboratory data as input) to evaluate the solubility of CO_2-N_2 gas mixtures in electrolyte solutions, demonstrated that higher water salinity is associated with reduced solubility of both CO_2 and N_2. However, the question remains whether complex aqueous solutions with identical IS but different compositions will dissolve the same amounts of CO_2 or exhibit different salting-out tendencies. Variations in dissolved CO_2 levels under identical IS conditions may arise due to differences in ion size or charge, pH, complex formation, mineral precipitation, or other chemical reactions.[42]

3.3. Speciation of Major, Minor, and Trace Elements during CO_2 Mineral Carbonation.

3.3.1. PP1 Aqueous Phase. Magnesium sulfate ($MgSO_4$) and SO_4^{2-} display the largest activities in the PP1 FGD-gypsum aqueous phase, followed in decreasing order by Mg^{2+} and $MnSO_4$. Among the solid phases encompassed in the LLNL database,[36] the geochemical modeling anticipates saturation at a pH of 6.30 aqueous phase, apart from $CaSO_4 \cdot 2H_2O$, in $NaAlSiO_3$, Al_2SiO_5, $AlOOH$, $Al(OH)_3$, Al_2O_3, SiO_2, $Mg_5Al_2Si_3O_{10}(OH)_8$, $Al_2Si_2O_5(OH)_4$, $KAlSi_3O_8$, $Na_2Al_2Si_3O_{10} \cdot 2H_2O$, $NaAl_3Si_3O_{10}(OH)_2$, Co_2SiO_4, $CoFe_2O_4$, $CuFeO_2$, $CuFe_2O_4$, $ZnFe_2O_4$, $Ca(UO_2)_2(Si_2O_5)_3 \cdot 5H_2O$, $CaAl_2Si_2O_7(OH)_2 \cdot H_2O$, $CaAl_2Si_2O_{10}(OH)_2$, $BaSO_4$, $Ca(UO_2)_2(VO_4)_2$, $UO_3 \cdot 9H_2O$, and KUO_2AsO_4 (Table S3). The occurrence of all supersaturated phases within the PP1 FGD-gypsum aqueous phase can be ascribed to the dissolution of elements originating from PP1 FGD-gypsum itself. During FGD, particles of FA, characterized by an Al−Si matrix, that enter undergo dissolution in the aqueous phase of the FGD-gypsum owing to the relatively alkaline conditions brought about by the neutralizer (limestone) within the FGD process. Once saturation is reached in the aqueous phase of the gypsum slurry, these elements tend to precipitate and/or coprecipitate.[39] The supersaturation of Co, Cu, and As species observed in the aqueous phase of PP1 FGD-gypsum can be elucidated by studying the behavior of these metals during combustion and their subsequent entry into the FGD system as well. During this process, moderately volatile elements such as Cu, Co, and As undergo condensation onto small particle surfaces carried within the flue gas stream,[34,35] which are subsequently entrapped by particulate control mechanisms, may, as previously noted, evade these controls, and ingress into the SO_2-enriched flue gas. They pass through the cooling and scrubbing zone, eventually integrating into the matrix of FGD-gypsum. Concerning As, it primarily undergoes a reaction as As_2O_3 with the ash conveyed in the flue gases, likely with CaO (at 500 °C), resulting in the formation of stable compounds,[45] such as $Ca_3(AsO_4)_2$, which then enter the FGD system.

3.3.2. PP2 Aqueous Phase. In the aqueous phase of the PP2 FGD-gypsum, Ca^{2+} and Mg^{2+} display the highest activity, followed by SO_4^{2-} and $CaSO_4$ in descending order (Table S3). The geochemical modeling, based on a pH of 7.29 and considering the solid phases in the LLNL database,[36] anticipates saturation of the FGD-gypsum aqueous phase in $Al(OH)_3$, $Mg_5Al_2Si_3O_{10}(OH)_8$, SiO_2, $KAlSi_3O_8$, $Na_2Al_2Si_3O_8$, $Fe(OH)_3$, $FeOOH$, Fe_2O_3, $KAl_3Si_3O_{10}(OH)_2$, and $Mg_3Si_4O_{10}(OH)_2$ (Table S3). The involvement of PP2 FGD-gypsum in the carbonation process is less impactful, attributed to its lower concentration of metallic impurities. This characteristic is also mirrored in the saturation index (SI), indicating a limited saturation of solid phases. At PP2, the particulate control mechanism relies on a bag filter system, which exhibits a comparable overall particle removal efficiency to an ESP but demonstrates superior efficiency in managing fine particulate matter.[46] Given that this fine particulate matter serves as a notable origin of trace elements in FGDs, employing the bag filter device would lead to reduced input of FA into the scrubber, consequently lowering the presence of metallic impurities. As for the PP1 FGD-gypsum, the presence of oversaturated Al−Si solid phases in the PP2 FGD-gypsum aqueous phase is due to the dissolution of solid species originating from PP2 FGD-gypsum itself.

3.3.3. PP3 Aqueous Phase. Calcium and Mg^{2+} show the highest activity in the PP3 FGD-gypsum aqueous phase followed in decreasing order by NO_3^- and $CaNO_3$. Based on the geochemical modeling at a pH of 6.83 and considering the solid phases listed in the LLNL database,[36] saturation of the aqueous phase is anticipated apart from Al−Si solid phases for $Ca_3Fe_2(SiO_4)_3$, $CaAl_2Si_4O_{12} \cdot 4H_2O$, $FeCa_2Al_2(OH)(SiO_4)_3$, $CaFe_2O_4$, $Ca(UO_2)_2(Si_2O_5)_3 \cdot 5H_2O$, $Ca_2Al_3Si_3O_{12}(OH)$, $CuFeO_2CuFe_2O_4$, $MgFe_2O_4$, $ZnFe_2O_4$, $BaSO_4$, $FeOOH$, Fe_2O_3, and $NiFe_2O_4$ (Table S3). As for the FGD-gypsums from PP1 and PP2, the occurrence of oversaturated Al−Si solid phases within the aqueous phase of PP3 FGD-gypsum stems from the dissolution of solid species originating directly from PP3 FGD-gypsum itself. The oversaturation of Ca species in the aqueous phase of the PP3 FGD-gypsum is ascribed to the saturation of aqueous complexes involving Ca, sourced by the neutralizing agent employed in the desulfurization process, in the FGD waters with metal impurities or from the dissolution of stable compounds (such as $Ca_3(AsO_4)$ or $CaFe_2O_4$) of FA that enter the FGD system. At postcombustion temperatures (500 °C), these stable compounds arise from interactions between alkaline earth oxides (such as CaO) and heavy metal oxides in the SO_2-rich flue gas that reach the scrubbing zone, representing a prevalent mechanism.[41]

3.3.4. Partitioning and Dynamics of Major and Trace Elements during CO_2 Conversion. The distribution of major and trace elements during CO_2 conversion was calculated by analyzing the concentrations of these elements in the input and output streams delineated in preceding sections, standardized according to their respective flow rates.

Consistent with these criteria, major and trace elements in the carbonation processes were categorized as follows:

Elements captured in the carbonation products (95−100%): Al, Fe, Si, Ca, Li, Ti, V, Cr, Mn, Zn, Cs (PP1), Ba, La, Ce, and U (PP1) and Nd (PP2 and PP3). These elements are introduced into the carbonation unit within the FGD-gypsum sludge and swiftly dissolve in the aqueous phase of the FGD-gypsum slurries as sulfate (e.g., $FeSO_4$, $CaSO_4$, $LiSO_4^-$, and $MgSO_4$) aqueous complexes and/or remain solvated, which leads to their

stability as free ions. As the carbonation progress, therefore, alkaline conditions are induced, these elements either as metal-HCO_3^-, metal-CO_3, and/or metal-hydroxide aqueous complexes become gradually more concentrated and eventually surpass their solubility limit and precipitate and/or coprecipitate in the carbonation products (Table S4). Aluminum and Si demonstrate distinct behavior as Al–Si solid species enter and partially dissolve in the aqueous phase of the gypsum slurry, associating with Na, ultimately precipitating as $NaAlSi_3O_8$. It is noteworthy that Al also forms associations with As, such as the $AlAsO_4 \cdot 2H_2O$ aqueous complex in the PP1 FGD-gypsum slurry. This speciation dynamics will be elaborated upon in detail in the following section.

Elements that form aqueous complexes in the carbonation slurries (90–100%): S. Sulfur produces a diverse range of metal-sulfate complexes within the aqueous milieu of the FGD-gypsum slurries. Throughout the carbonation process, it predominantly persists in a stable state as a SO_4^{2-} and as aqueous complexes such as Na_2SO_4 and $MgSO_4$ (Table S4).

Elements are retained within the carbonation end-products to a significant extent (60–80%), with a substantial portion found in the aqueous phases (20–40%): Mg (PP1). Magnesium is mostly present in the FGD-gypsum slurries as $MgSO_4$ aqueous complex. As the carbonation progresses, Mg can exist in both the aqueous phases of the carbonation products as aqueous complexes such as MgOH, $MgCO_3$, and $MgSO_4$ and be retained in the carbonate end-products as dolomite ($CaMg(CO_3)$) (Table S4).

In addition to producing carbonation products, the carbonation process also generates an aqueous phase that is notably enriched in Na_2SO_4 (Table S5, Supporting Information). Sodium sulfate, due to its versatile chemical properties, finds application in various industries. It is commonly utilized in the production of detergents as a key ingredient for enhancing cleaning efficiency. In textile industries, sodium sulfate aids in the dyeing process by facilitating the uniform absorption of dyes onto fabrics. Moreover, it plays a crucial role in the refining of glass, helping to remove impurities and ensuring the production of high-quality glass products. These applications highlight sodium sulfate's broad utility across different sectors.

By scrutinizing the chemical composition and speciation at each stage of CO_2 conversion, we were able to propose four potential pathway reactions that govern the eventual speciation of these elements:

i. Conversion of metal sulfates to metal carbonate (metal-CO_3) complexes: Elements that associate with SO_4^{2-} form aqueous complexes (e.g., $LaSO_4^+$, $MnSO_4$, $SrSO_4$, and YSO_4^+/$Y(SO_4)^{2-}$) and/or remain solvated, which leads to their stability as free ions (e.g., Ce^{3+} and Pb^{2+}) during the initial stage of the process. As carbonation progresses, these elements begin to partially associate with HCO_3^-, OH^-, and/or CO_3^{2-} ions. This association alters their chemical environment and affects their solubility. Eventually, as the concentrations of these ions increase and the system reaches supersaturation, the elements surpass their solubility thresholds and precipitate as solid carbonate species. This precipitation process reduces their mobility and can significantly influence the overall carbonation efficiency by altering the composition and purity of the resulting $CaCO_3$. This behavior is followed by Pb and U in the PP1 CO_2 conversion and by Sr, Mn, La, Y, and Ce in the PP1, PP2, and PP3 CO_2 conversion, which precipitate in the carbonation product as $SrCO_3$, $MnCO_3$, $La_2(CO_3)_3 \cdot 8H_2O$, $Ce_2(CO_3)_3 \cdot 8H_2O$, $Y_2(CO_3)_3$, and $PbCO_3$ (SI provided in Table S3).

ii. Transformation of transferable elements into metal oxides and oxyhydroxide (metal-Ox/metal-XO_xOH^{x-n}) complexes: Elements that initially stabilize as free hydroxy-oxo-metal ions (e.g., $H_2VO_4^-$) and/or as oxyhydroxide complexes (e.g., $XO-OH^{x-n}$) undergo significant changes as carbonation progresses. During the initial stage, these elements maintain their stability in these forms. However, as the carbonation process advances, the increasing concentrations of ions and changing chemical conditions may lead these elements to surpass their solubility thresholds. Consequently, they may coprecipitate either as oxides or oxyhydroxide solid species. This transition from a soluble to a precipitated state affects the overall dynamics of the system, influencing both the efficiency of the carbonation process and the composition of the resulting solid products. This behavior is followed by V in the PP1 CO_2 conversion, which coprecipitates in the carbonation product as V_2O_5 (Table S3).

iii. Transformation of metal sulfates into diverse metal complexes: Elements that associate with SO_4^{2-} to form aqueous complexes (e.g., $MgSO_4$, $ZnSO_4$, UO_2SO_4) hydroxide complexes (e.g., $CrOH^{2+}$, $Ti(OH)_4$, and $UO_2(OH)_2$) and/or remain solvated as free ions (e.g., Ba^{2+}) exhibit stability in these forms during the initial stage of the process. As carbonation progresses, these elements begin to partially associate with HCO^{3-}, OH^-, and/or CO_3^{2-} ions. This association changes their chemical environment, leading them to eventually precipitate or coprecipitate as a diverse array of solid species within the carbonation products. This transformation from soluble complexes and free ions to solid precipitates affects the overall composition and characteristics of the final carbonation products, influencing both the efficiency and the nature of the carbonation process. This behavior is followed by Mg in the PP1 and PP3 and Cr, Ti, and Ba in the PP1, PP2, and PP3 CO_2 conversion, which precipitate in the carbonate end-product as $MgCO_3$, $Mg_2CO_3(OH)_2 \cdot 3H2O$, $CaMg(CO_3)_2$, $Mg_5(CO_3)_4(OH)_2 \cdot 4H_2O$, $Mg_2Cl(OH)_3 \cdot 4H_2O$, $Mg(OH)_2$, $BaCa(CO_3)_2$, $BaCO_3$, $CuCr_2O_4$, Cr_2O_3, $ZnCr_2O_4$, TiO_2, Zn_2TiO_4, $ZnCO_3$, and $ZnCO_3 \cdot H_2O$ (Table S3).

iv. Diverse pathways of elemental transformation: Iron, Al, and As do not conform to any of the three pathway reactions described. It is noteworthy that the speciation analysis indicates that these three elements, which deviate from the described trends, are initially associated at the onset of mineral carbonation. The distinctive behavior and interplay governing their final speciation during CO_2 conversion are thoroughly examined in the following sections, aimed at elucidating the dynamics of As in the mineral carbonation process described in the paper.

3.4. Dynamics of As during CO_2 Conversion. In the initial of all FGD-gypsum slurry aqueous phases, particularly in the PP1 FGD-gypsum, As forms a range of aqueous complexes with metals. Among these, the most active complexes are $Mn_3(AsO_4)_2 \cdot 8H_2O$ in PP1 and $AlAsO_4 \cdot 2H_2O$ in PP2 and PP3 (Figure 5a–c). This phenomenon arises from the significant presence of metal impurities that dissolve from the FGD-
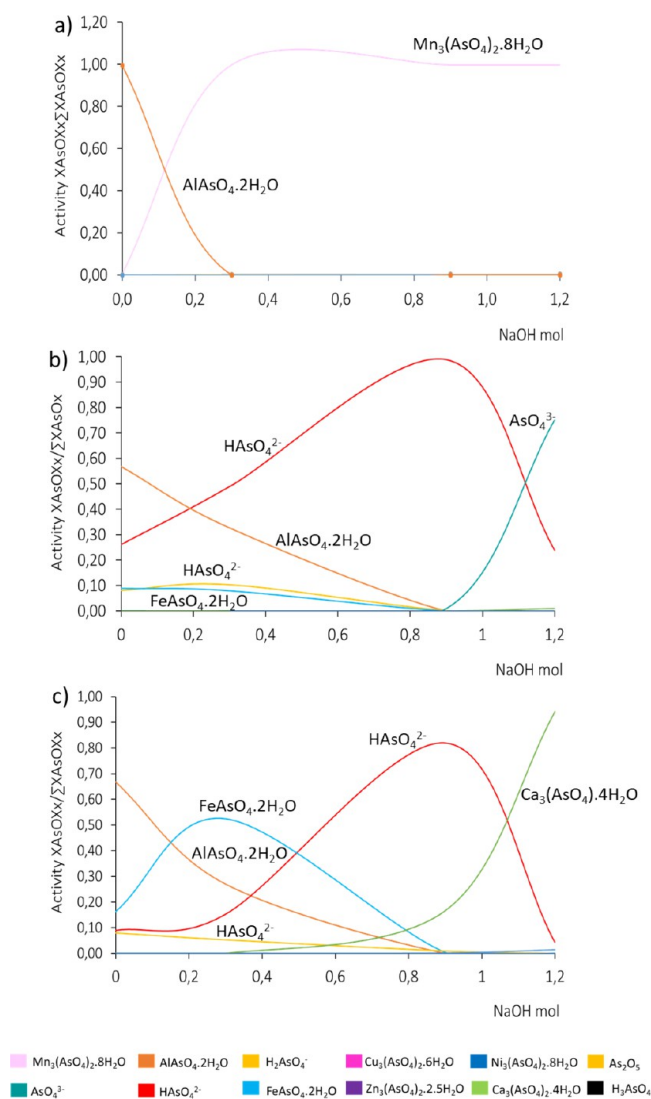
Figure 5. Diagrams of stability of As complexes during the PP1 (a), PP2 (b), and PP3 (C) CO_2 conversions as a function of NaOH dosages and CO_2 injection. The initial solutions are the PP1, PP2, and PP3 FGD-gypsum aqueous phases, respectively.

gypsum itself. As elucidated throughout the paper, FGD systems typically maintain both alkaline and oxidizing conditions to facilitate the neutralization of SO_2-rich flue gas, followed by oxidation to form $CaSO_4 \cdot 2H_2O$. These conditions impact all elements present in the scrubber. In the case of As, its retention in the FGD-gypsum matrix likely occurs as $Ca_3(AsO_4)_2$, which subsequently dissolves once the gypsum slurry is generated. Under these relatively alkaline conditions, AsO_4^{3-} interacts with metals in solution, forming the aforementioned metallic complexes (Figure 5a−c).

As evident from the stability diagrams, $Mn_3(AsO_4)_2 \cdot 8H_2O$ is the only complex that not only maintains its activity but even shows a slight increase as the carbonation process progresses in PP1 (Figure 5a). Conversely, other complexes such as $Cu_3(AsO_4)_2 \cdot 8H_2O$ and $Zn_3(AsO_4)_2 \cdot 8H_2O$ experience a decrease in activity due to the formation of new associations with either HCO_3^- or CO_3^{2-} such as $Cu(CO_3)_2^{2-}$ and $ZnHCO_3^+$, respectively. In PP2, the impact of FGD-gypsum on the carbonation process is diminished, attributed to its lower concentration of metallic impurities. This trend is also evident in

the stability diagrams, where the activity of most metallic impurities decreases as they form complexes with CO_3^{2-} and HCO_3^-, while AsO_4^{3-} remains stable after the completion of carbonation (Figure 5b). In the course of PP3 CO_2 conversion, the $Ca_3(AsO_4)_2 \cdot 8H_2O$ aqueous complex initially demonstrates lower activity compared to other metallic-AsO_4^{3-} or H_xAsO_x complexes present in the gypsum slurry (Figure 5c). However, its activity gradually escalates as the carbonation process approaches completion. A comparison of the Ca/Mn, Ca/Fe, and Ca/Al ratios between PP3 and PP2 FGD-gypsum slurries reveals a higher proportion of Ca relative to Mn (>2000), Fe (>30000), and Al (>1500) in the PP3 FGD-gypsum.

This difference contributes to the heightened activity of $Ca_3(AsO_4)_2 \cdot 8H_2O$ in PP3 because of the lower input of Mn, Fe, and Al and the reduced load of metallic impurities compared to PP2. Conversely, the concentration of Ca in the PP1 gypsum slurry surpasses that of M only by a factor of 0.576. Considering that most of the available Ca^{2+} reacts primarily with HCO_3^- and CO_3^{2-} to complete mineral carbonation, the significant concentration of Mn (1027 mg/L) also allows Mn to be available for forming $Mn_3(AsO_4)_2 \cdot 8H_2O$, which prevails throughout the PP1 complete carbonation process.

No As species reach saturation in the aqueous phases of the carbonation products, consistent with the absence of As in the carbonation products of PP2 and PP3. However, trace amounts of As are detected in the carbonation product of PP1. The retention of As in the PP1 carbonate end-product can be attributed to coprecipitation processes, where As substitutes for other ions in the crystal lattice of a primary compound. This phenomenon commonly occurs when the coprecipitated element shares similar chemical properties and ionic sizes with the primary element. Arsenic can also be retained in the PP1 carbonation product through adsorption onto the surface of growing particles or occlusion within precipitate particles.

Particular emphasis should be placed on the initial association of AsO_4^{3-} with Al (Table 3). Contrasting most elements, Al does not form associations with either HCO_3^- or CO_3^{2-} due to the high instability of these aqueous complexes and solid species. The Al^{3+} ion and CO_3^{2-} ion exhibit significant differences in size (Al^{3+} is small while CO_3^{2-} is bulky), impacting the reticular stability of the crystal lattice. This results in inadequate interaction between ions if this salt were to be isolated in the solid state.[47] Additionally, Al^{3+} is a highly polarizing cation, deforming the electronic cloud of CO_3^{2-}. Consequently, ionic interactions between Al^{3+} and CO_3^{2-} tend toward covalence, further contributing to the instability of $Al_2(CO_3)_3$. Consequently, during the PP1 CO_2 conversion without alkaline induction, Al and As form the complex $AlAsO_4 \cdot 2H_2O$. This aqueous complex exhibits the highest activity among the As complexes in PP3 and ranks second in the aqueous complexes of PP2 (Table 3). However, interaction between Al^{3+} and CO_3^{2-} may occur in the presence of Na^+ and OH^- ions (alkaline induction), leading to the formation of stable crystals such as $NaAlCO_3(OH)_2$ (Dawsonite). This explains the decrease of the $AlAsO_4 \cdot 2H_2O$ aqueous complex during the CO_2 conversions.

In the carbonated end-products, $NaAlCO_3(OH)_2$ and $AlOOH$ (boehmite) are the coprecipitated Al species, with AlO_2^- and $NaAlO_2$ being the predominant aqueous complexes during CO_2 conversion (Table 3). AlO_2^- is formed from Al^{3+} hydrolysis along with the liberation of H^+ into the medium.

In PP1 CO_2 conversion, Fe initially exhibits its highest activity as $FeSO_4$, followed by Fe^{2+}, $FeAsO_4 \cdot 2H_2O$, $Fe(OH)_2^+$, and $Fe(OH)_3$ aqueous complexes (Table 3). As alkaline conditions

Table 3. Activity of Fe and Al Aqueous Complexes during the Phases of the PP1, PP2, and PP3 Mineral Carbonation Process CO_2 Conversions as a Function of NaOH Dosages and CO_2 Injection[a]

Activity	PP1				PP2				PP3			
	*FGD-gypsum	Alkaline induction	CO_2 injection	Carbonation	*FGD-gypsum	Alkaline induction	CO_2 injection	Carbonation	*FGD-gypsum	Alkaline induction	CO_2 injection	Carbonation
$FeSO_4$	1.03×10^{-07}	6.73×10^{-06}	3.35×10^{-06}	3.35×10^{-06}	1.27×10^{-04}	2.91×10^{-05}	9.18×10^{-06}	9.18×10^{-06}	1.11×10^{-04}	4.73×10^{-13}	1.29×10^{-15}	1.50×10^{-21}
Fe^{2+}	2.18×10^{-08}	1.27×10^{-06}	2.91×10^{-06}	2.91×10^{-06}	6.12×10^{-04}	5.45×10^{-05}	3.41×10^{-05}	3.41×10^{-05}	6.21×10^{-04}	2.42×10^{-12}	5.88×10^{-15}	6.22×10^{-21}
$FeAsO_4 \cdot 2H_2O$	2.31×10^{-10}	6.76×10^{-11}	7.16×10^{-12}	7.16×10^{-12}	1.66×10^{-06}				1.66×10^{-06}	4.43×10^{-06}	1.03×10^{-08}	2.89×10^{-16}
$Fe(OH)_2^+$	1.69×10^{-10}	2.41×10^{-09}	1.81×10^{-09}	1.81×10^{-09}	4.71×10^{-04}	6.90×10^{-04}	1.36×10^{-05}	1.36×10^{-05}	5.77×10^{-05}	2.80×10^{-04}	9.95×10^{-06}	8.39×10^{-10}
$Fe(OH)_3$	1.54×10^{-10}	2.56×10^{-08}	7.72×10^{-08}	7.72×10^{-08}	1.18×10^{-03}	1.05×10^{-03}	1.04×10^{-03}	1.04×10^{-03}	1.82×10^{-04}	2.23×10^{-03}	2.24×10^{-03}	5.24×10^{-05}
$FeOH^+$	1.34×10^{-11}	9.14×10^{-09}	3.91×10^{-08}	3.91×10^{-08}	3.76×10^{-06}	1.21×10^{-06}	6.42×10^{-06}	6.42×10^{-06}				
Fe^{3+}	2.09×10^{-17}	2.18×10^{-18}	8.29×10^{-08}	8.29×10^{-08}	5.84×10^{-13}	6.83×10^{-12}	1.79×10^{-17}	1.79×10^{-17}	5.95×10^{-13}	4.50×10^{-13}	2.01×10^{-17}	2.20×10^{-26}
$FeHCO_3^+$	0.00×10^{00}	0.00×10^{00}	1.17×10^{-04}	1.33×10^{-04}	0.00×10^{00}		1.63×10^{-03}	3.07×10^{-04}	0.00×10^{00}	0.00×10^{00}	1.04×10^{-10}	8.43×10^{-21}
$FeCO_3$	0.00×10^{00}	0.00×10^{00}	1.32×10^{-05}	6.16×10^{-05}	0.00×10^{00}		2.32×10^{-04}	2.09×10^{-03}	0.00×10^{00}	0.00×10^{00}	8.58×10^{-12}	1.97×10^{-18}
$Fe(OH)_4^-$					2.09×10^{-05}	2.95×10^{-05}	5.66×10^{-04}	5.66×10^{-04}	3.07×10^{-07}	9.57×10^{-06}	2.71×10^{-04}	1.76×10^{-03}
$FeCl^+$									9.03×10^{-07}	3.44×10^{-15}	8.28×10^{-18}	8.56×10^{-24}
$AlAsO_4 \cdot 2H_2O$	1.31×10^{-04}	7.91×10^{-08}	4.70×10^{-10}	4.70×10^{-10}					6.85×10^{-06}	2.29×10^{-06}	5.53×10^{-10}	2.33×10^{-18}
AlO_2^-	5.97×10^{-05}	2.46×10^{-04}	2.57×10^{-04}	2.57×10^{-04}	1.19×10^{-02}	1.15×10^{-02}	1.16×10^{-02}	1.11×10^{-02}	1.70×10^{-03}	6.71×10^{-03}	2.00×10^{-02}	1.95×10^{-02}
$HAlO_2$	8.74×10^{-05}	3.04×10^{-05}	5.22×10^{-06}	5.22×10^{-06}	1.78×10^{-03}	1.18×10^{-03}	9.60×10^{-06}	2.65×10^{-08}	7.35×10^{-04}	1.14×10^{-03}	1.19×10^{-04}	4.19×10^{-07}
$Al(OH)_2^+$	3.01×10^{-05}	8.82×10^{-07}	2.50×10^{-08}	2.50×10^{-08}	6.25×10^{-05}	2.82×10^{-05}	1.87×10^{-09}	1.49×10^{-14}	7.47×10^{-05}	4.54×10^{-05}	1.68×10^{-07}	2.12×10^{-12}
$AlOH^{2+}$	6.66×10^{-06}	1.67×10^{-08}	7.89×10^{-11}	7.89×10^{-11}	1.38×10^{-06}	4.28×10^{-07}	2.30×10^{-13}	5.33×10^{-21}	4.78×10^{-06}	1.15×10^{-06}	1.50×10^{-10}	6.84×10^{-18}
$Al(SO_4)_2^-$	2.14×10^{-05}	5.81×10^{-09}	4.94×10^{-12}	4.94×10^{-12}	1.05×10^{-08}	8.60×10^{-10}	2.15×10^{-18}	8.25×10^{-29}	6.39×10^{-09}	7.21×10^{-10}	4.24×10^{-15}	8.40×10^{-25}
$AlSO_4^+$	9.28×10^{-06}	2.24×10^{-09}	1.84×10^{-12}	1.84×10^{-12}	2.96×10^{-08}	3.90×10^{-09}	1.29×10^{-17}	6.55×10^{-28}	7.30×10^{-08}	7.55×10^{-09}	3.94×10^{-14}	7.11×10^{-24}
Al^{3+}	3.05×10^{-07}	6.57×10^{-11}	5.17×10^{-14}	5.17×10^{-14}	6.33×10^{-09}	1.34×10^{-09}	5.89×10^{-18}	3.95×10^{-28}	6.33×10^{-08}	5.99×10^{-09}	2.78×10^{-14}	4.57×10^{-24}
$NaAlO_2$	2.43×10^{-07}	1.44×10^{-05}	2.70×10^{-05}	2.70×10^{-05}	1.16×10^{-06}	2.79×10^{-04}	5.22×10^{-04}	7.39×10^{-04}	1.80×10^{-06}	1.67×10^{-04}	9.61×10^{-04}	1.43×10^{-03}

[a]The initial solutions are the PP1, PP2, and PP3 FGD-gypsum aqueous phases.

are introduced and CO_2 diffuses into the aqueous phase, $FeHCO_3^+$ and $FeCO_3$ gradually become predominant (pH $\approx$ 7.37−8.15). Meanwhile, the activity of Fe^{3+} and $FeOH^+$ also increases gradually, and $FeCO_3$ precipitates as the carbonate end-products, with Fe_2O_3 and $FeOOH$ precipitating. In PP2 CO_2 conversion, $Fe(OH)_3$, Fe^{2+}, and $Fe(OH)_2^+$ predominate initially, followed by the emergence of $FeHCO_3^-$ and $FeCO_3$ as the predominant aqueous complexes. $FeHCO_3^-$ declines as $FeCO_3$ reaches saturation, and $Fe(OH)_4^-$ activity rises in the carbonate end-product due to unfavorable thermodynamic stability conditions. In PP3 CO_2 conversion, Fe^{2+} and $Fe(OH)_3$ initially prevail, with $Fe(OH)_3$ activity increasing markedly upon CO_2 introduction. $FeHCO_3^-$ and $FeCO_3$ coexist at varying activity levels, along with Fe^{3+}, $FeCO_3$, and $FeOH^+$. The solid Fe species precipitated include $FeOOH$ (goethite), $CaFe_2O_4$ (ferrite-Ca), and hematite (Fe_2O_3).

4. CONCLUSIONS

In this study, we assessed metal impurity partitioning and speciation in mineral carbonation processes using FGD-gypsum from coal-fired power plants in Spain and China.

XRD analysis revealed that the carbonation product from PP1 FGD-gypsum is primarily single-phase $CaCO_3$ crystals. In contrast, PP2 and PP3 FGD-gypsum carbonation products contained $CaCO_3$ along with undesirable intermediate phases like $CaSO_3$, $Na_6CO_3(SO_4)_2$, and $CaMg(CO_3)$. Additionally, the PP3 product included quartz, inherited from the parent gypsum.

PP1 and PP2 carbonation products had $CaCO_3$ content ranging from 81 to 83%, whereas PP3 had 76.9%. This variance is due to undissolved impurities such as SiO_2, intermediate phases formed during carbonation, and a significant influx of NO_3^- during CO_2 conversion, which increased ionic strength and competition for Ca ions.

Our analysis identified four potential reaction pathways governing carbonation efficiency: (i) conversion to metal carbonates, (ii) transformation into metal oxides and oxyhydroxides, (iii) transformation into metal multiform compounds, and (iv) diverse pathways of elemental transformation.

Arsenic formed complexes with metals, such as $Mn_3(AsO_4)_2\cdot 8H_2O$ in PP1 and $AlAsO_4\cdot 2H_2O$ in PP2 and PP3, influenced by the concentration of Mn, Fe, and Al. Higher Ca/Mn, Ca/Fe, and Ca/Al ratios in PP3 enhanced $Ca_3(AsO_4)_2\cdot 8H_2O$ activity, while in PP1, excess Ca facilitated $Mn_3(AsO_4)_2\cdot 8H_2O$ formation. Coprecipitation retained As in PP1 carbonate products due to similar chemical properties with primary compounds.

Though trace element phases expected to reach saturation were not detected by XRD, the identified structural constituents supported the precipitation mechanisms of metal species as carbonates, oxides, and/or oxyhydroxides in the carbonation products of PP1, PP2, and PP3.

Using FGD-gypsum in carbonation processes appears viable in the lab, but metal impurities in FGD-gypsum can significantly affect CO_2 conversion efficiency and the feasibility of using carbonation end-products. This has implications for environmental leaching and reuse potential. Therefore, it is crucial to implement effective measures to reduce metal impurities in FGD-gypsum before using it as a Ca source for converting CO_2 into stable carbonates. This can be achieved through refining processes or technologies that minimize the risk of introducing undesirable elements during CO_2 conversion. While prioritizing purity is essential for CO_2 conversion, it is imperative to balance the costs and benefits, considering both improvements in conversion efficiency and the quality of the resulting carbonates.

Future research will focus on evaluating the mobility of these impurities and their viability as raw materials for concrete production.

■ ASSOCIATED CONTENT

Ⓢ Supporting Information

The Supporting Information is available free of charge at https://pubs.acs.org/doi/10.1021/acsomega.4c04958.

> Operating conditions during the carbonation experiments; flow rates of input and output streams involved in the CO_2 conversions; impact of metal impurities on the PP1, PP2, and PP3 carbonation efficiency; saturation indices of a set of minerals in the carbonate slurries; reactions involved during CO_2 conversion; concentration of major, minor, and trace elements in the aqueous phase of the PP1, PP2, and PP3 carbonation slurries (PDF)

■ AUTHOR INFORMATION

Corresponding Author

Patricia Córdoba − *Institute of Environmental Assessment and Water Research (IDÆA-CSIC), Spanish National Research Council, Barcelona 08034, Spain;* Ⓘ orcid.org/0000-0003-0596-4354; Email: patricia.cordoba@idaea.csic.es

Complete contact information is available at:
https://pubs.acs.org/10.1021/acsomega.4c04958

Notes

The author declares no competing financial interest.

■ REFERENCES

(1) Global Energy Monitor, 2023. *Center for Research on Energy and Clean Air.* https://energyandcleanair.org/wp/wp-content/uploads/2023/02/CREA_GEM_China-permitstwo-new-coal-power-plants-per-week-in-2022.pdf.

(2) International Energy Agency (EIA), 2023, https://www.iea.org/energy-system/fossil-fuels/coal.

(3) You, C.; Xu, X. Coal combustion and its pollution control in China. *Energy.* **2010**, *35* (11), 4467−4472.

(4) Tan, Y.; Nookuea, W.; Li, H.; Thorin, E.; Yan, J. Property impacts on carbon capture and storage (CCS) processes: a review. *Energy Convers. Manag.* **2016**, *118*, 204−222.

(5) Wang, F.; Dresinger, D. An integrated process of CO_2 mineralization and selective nickel and cobalt recovery from olivine and laterites. *Chem. Eng. J.* **2023**, *451*, No. 139002.

(6) Wang, F.; Dreisinger, D.; Xiao, Y. Accelerated CO_2 mineralization and utilization for selective battery metals recovery from olivine and laterites. *J. Cleaner Prod.* **2023**, *393*, No. 136345.

(7) Kang, C.-U.; Ji, S.-W.; Jo, H. Recycling of Industrial Waste Gypsum Using Mineral Carbonation. *Sustainability* **2022**, *14*, 4436.

(8) Mattila, H.-P.; Zevehoven, R. Mineral Carbonation of Phosphogypsum Waste for Production of Useful Carbonate and Sulfate Salts. *Front. Energy Res.* **2015**, *3* (3), 48.

(9) Azdarpour, A.; Asadullah, M.; Junin, R.; Manan, M.; Hamidi, H.; Mohammadian, E. Direct carbonation of red gypsum to produce solid carbonates. *Fuel Process. Technol.* **2014**, *126*, 429−434.

(10) Kamarudin, R. A.; Zakaria, M. S. The utilization of red gypsum waste for glazes. *Malays. J. Anal. Sci.* **2007**, *11*, 57−64.

(11) Azdarpour, A.; Afkhami Karaei, M.; Hamidi, H.; Mohammadian, E.; Honarvar, B. CO₂ sequestration through direct aqueous mineral carbonation of red gypsum. *Petroleum.* **2018**, *4*, 398−407.

(12) Kikkawa, H.; Nakamoto, T.; Morishita, M.; Yamada, K. New wet FGD process using granular limestone. *Ind. Eng. Chem. Res.* **2002**, *41*, 3028−3036.

(13) Harder, J. *Gypsum − a sarce raw material?* https://www.at-minerals.com/en/artikel/at_gypsum_a_scarce_raw_material_-3752853.html.

(14) Wang, B.; Pan, Z. H.; Du, Z. P.; Cheng, H. G.; Cheng, F. Q. Effect of impure components in flue gas desulfurization (FGD) gypsum on the generation of polymorph CaCO₃ during carbonation reaction. *J. Hazard. Mater.* **2019**, *369*, 236−243.

(15) Huijgen, W. J.; Comans, R. N. Carbonation of steel slag for CO2 sequestration: leaching of products and reaction mechanisms. *Environ. Sci. Technol.* **2006**, *40*, 2790−2796.

(16) Bodor, M.; Santos, R. M.; Gerven, T. V.; Vlad, M. Recent developments and perspectives on the treatment of industrial wastes by mineral carbonation — a review. *Open Eng.* **2013**, *3*, 566−584.

(17) Olajire, A. A. A review of mineral carbonation technology in sequestration of CO₂. *J. Petrol. Sci. Eng.* **2013**, *109*, 364−392.

(18) Sanna, A.; et al. Waste materials for carbon capture and storage by mineralisation (CCSM) − a UK perspective. *Appl. Energy* **2012**, *99*, 545.

(19) Power, I. M.; Harrison, A. L.; Dipple, G. M.; Wilson, S.; Kelemen, P. B.; Hitch, M.; Southam, G. Carbon mineralization: from natural analogues to engineered systems. *Rev. Mineral. Geochem.* **2013**, *77*, 305−360.

(20) Li, J.; Jacobs, A. D.; Hitch, M. Direct aqueous carbonation on olivine at a CO₂ partial pressure of 6.5 MPa. *Energy* **2019**, *173*, 902−910.

(21) Dlugogorski, B. Z.; Balucan, R. D. Dehydroxylation of serpentine minerals: Implications for mineral carbonation. *Renew. Sustain. Energy Rev.* **2014**, *31*, 353−367.

(22) Sun, J.; Liu, W.; Wang, W.; Hu, Y.; Yang, X.; Chen, H.; Zhang, Y.; Li, X.; Xu, M. Optimizing synergy between phosphogypsum disposal and cement plant CO₂ capture by the calcium looping process. *Energy Fuels* **2016**, *30*, 1256−1265.

(23) Ghacham, A. B.; Pasquier, L. C.; Cecchi, E.; Blais, J. F.; Mercier, G. Valorization of waste concrete through CO₂ mineral carbonation: Optimizing parameters and improving reactivity using concrete separation. *J. Cleaner Prod.* **2017**, *166*, 869−878.

(24) Zevenhoven, R.; Fagerlund, J.; Songok, J. K. CO₂ mineral sequestration: developments towards large-scale application. *Greenhouse Gases* **2011**, *1*, 48−57.

(25) Snæbjörnsdóttir, S.Ó.; Sigfússon, B.; Marieni, C.; et al. Carbon dioxide storage through mineral carbonation. *Nat. Rev. Earth Environ.* **2020**, *1*, 90−102.

(26) Wang, B.; Pan, Z.; Cheng, H.; Zhang, Z.; Cheng, F. A review of carbon dioxide sequestration by mineral carbonation of industrial by-product gypsum. *Journal of Cleaner Production.* **2021**, *302*, No. 126930.

(27) Córdoba, P.; Rojas, S. Carbon sequestration through mineral carbonation: Using commercial FGD-gypsum from a copper smelter for sustainable waste management and environmental impact mitigation. *Journal of Environmental Chemical Engineering.* **2024**, *12* (2), No. 112510.

(28) Córdoba, P.; Ayora, C.; Querol, X. Evaluation of chemical stabilisation methods of coal-petcoke fly ash to reduce the mobility of Mo and Ni against environmental concerns. *Ecotoxicology and Environmental Safety.* **2021**, *208*, No. 111488.

(29) Córdoba, P.; Li, B.; Li, J.; Zhuang, X.; Querol, X. Chemical Speciation and Leaching Behavior of Hazardous Trace Elements in Coal Combustion Products from Coal-Fired Power Stations in China. *ACS. Omega.* **2022**, *7* (17), 14697−14711.

(30) Querol, X.; Alastuey, A.; Chinchón, J. S.; Fernández, J. L.; López, A., 2nd Report7220/Ed/014 *European Coal and Steel Community Project*, 1993.

(31) Lee, M. G.; Jang, Y. N.; Ryu, K. W.; Kim, W.; Bang, J. Mineral carbonation of flue gas desulfurization gypsum for CO₂ sequestration. *Energy.* **2012**, *47*, 370−377.

(32) Maroto-Valer, R.; Winkel, H.; Gimenez, A.; Fernandez, C.; Martínez-Tarazona, R.; Querol, X.; Ballesteros, J. C.; Koukouzas, N. European Commission (EC), Directorate-General for Research and Innovation. *Abatement of Emissions of Trace Pollutants by FGD from co-combustion and environmental characteristics of by-products (ABETRAP)*. Research Programme of the Research Fund for Coal and Steel (RFCR). RFCR-CT-2006−00006 2006−2010.

(33) Córdoba, P.; Ochoa-Gonzalez, R.; Font, O.; Izquierdo, M.; Querol, X.; Leiva, C.; López-Antón, M. A.; Díaz-Somoano, M.; Rosa Martinez-Tarazona, M.; Fernandez, C.; Tomás, A. Partitioning of trace inorganic elements in a coal-fired power plant equipped with a wet flue gas desulphurisation system. *Fuel* **2012**, *92*, 145−157.

(34) Córdoba, P.; Font, O.; Izquierdo, M.; Querol, X.; Leiva, C.; López-Antón, M. A.; Díaz-Somoano, M.; Ochoa-González, R.; Rosa Martinez-Tarazona, M.; Gómez, P. The retention capacity for trace elements by the flue gas desulphurisation system under operational conditions of a co-combustion power plant. *Fuel* **2012**, *102*, 773−788.

(35) Tabasová, A.; Kropáč, J.; Kermes, V.; Nemet, A.; Stehlík, P. Waste-to-energy technologies: Impact on environment. *Energy* **2012**, *44*, 146−155.

(36) Parkhurst, D. L.; Appelo, C. A. J. User's guide to PHREEQC (version 2): A computer program for speciation, reaction path, 1D transport, and inverse geochemical calculations. *U.S. Geol. Surv. Water Resour. Invest. Rep.* **1999**, 99−4259.

(37) Clarke, L. B.; Sloss, L. L. *Trace elements: emissions from coal combustion and gasification.* IEACR/49, 1992. IEA Coal Research. ISBN 92−9029−204−0.

(38) Tumati, P. R.; Devito, M. S. Retention of condensed/solid phase trace elements in an electrostatic precipitator. Paper presented at the *Proceeding of the 1st EPRI Conference: Managing Hazardous Air Pollutants: Sate of the Art*, 1991, Washington DC, US, 20 pp.

(39) Córdoba, P.; Font, O.; Izquierdo, M.; Querol, X.; Tobías, A.; López-Antón, M.; Ochoa-González, R.; Díaz-Somoano, M.; Martínez-Tarazona, M.; Ayora, C.; Leiva, C.; Fernández, C.; Giménez, A. Enrichment of inorganic trace pollutants in re-circulated water streams from a wet limestone flue gas desulphurisation system in two coal power plants. *Fuel Process. Technol.* **2011**, *92*, 1764−1775.

(40) Maciejewski, M. Computational aspects of kinetic analysis. Part B: the ICTAC kinetic project − the decomposition kinetics of calcium carbonate revisited, or some tips on survival in the kinetic minefield. *Thermochim. Acta* **2000**, *355*, 145−154.

(41) Kwon, S.; Messing, G. L. The effect of particle solubility on the strength of nanocrystalline agglomerates: Boehmite. *Nanostructured Materials* **1997**, *8* (4), 399−418.

(42) Iskra, K.; Krawczyk, L.; Miodoński, J. M.; Wierzbicka-Kopertowska, D. Nitrate removal from wastewater generated in wet Flue Gas Desulphurisation Systems (FGD) in coal-fired power generation using the heterotrophic denitrification method. Environmental Protection and Natural. *Resources.* **2020**, *31* (3), 27−34.

(43) Gilbert, K.; Bennett, P. C.; Wolfe, W.; Zhang, T.; Romanak, K. D. CO₂ solubility in aqueous solutions containing Na⁺, Ca²⁺, Cl⁻, SO₄²⁻ and HCO₃⁻: The effects of electrostricted water and ion hydration thermodynamics. *Appl. Geochem.* **2016**, *67*, 59.

(44) Nakhaei-Kohani, R.; Taslimi-Renani, E.; Hadavimoghaddam, F.; et al. Modeling solubility of CO₂−N₂ gas mixtures in aqueous electrolyte systems using artificial intelligence techniques and equations of state. *Sci. Rep.* **2022**, *12*, 3625.

(45) Gutberlet, H. Influence of furnace type on poisoning Of DENOx catalyst by arsenic. *VGB Kraftwerkstech.* **1988**, *68*, 264−271.

(46) Meuleman, E. A.; Cottrell, A.; Ghayur, A. Treatment of flue-gas impurities for liquid absorbent-based post-combustion CO₂ capture processes. *Absorption-Based Post-combustion Capture of Carbon Dioxide.* **2016**, 519−551.

(47) Rumble, J. R. *Handbook of chemistry and physics*; T&F, CRC Press; N° 102 edición 2021.